Title

Tailoring Morphology of Cu–Ag Nanocrescents and Core–Shell Nanocrystals Guided by a Thermodynamic Model

Journal

Journal of the American Chemical Society, 140(27)

ISSN

0002-7863

Authors

Osowiecki, Wojciech T
Ye, Xingchen
Satish, Pratima
et al.

Publication Date

2018-07-11

DOI

10.1021/jacs.8b04558

Peer reviewed

Tailoring Morphology of Cu-Ag Nanocrescents and Core-Shell Nanocrystals Guided by a Thermodynamic Model

Wojciech T. Osowiecki[1,2], Xingchen Ye[2], Pratima Satish[2], Karen C. Bustillo[5], Ezra L. Clark[6,7], A. Paul Alivisatos[1-4]

[1]Materials Sciences Division, Lawrence Berkeley National Laboratory, Berkeley, CA 94720, USA.

[2]Department of Chemistry, University of California, Berkeley, California 94720, USA.

[3]Department of Materials Science and Engineering, University of California, Berkeley, California 94720, USA.

[4]Kavli Energy NanoScience Institute, Berkeley, California 94720, USA.

[5]National Center for Electron Microscopy, Molecular Foundry, Lawrence Berkeley National Laboratory, Berkeley, California 94720, USA.

[6]Joint Center for Artificial Photosynthesis, Lawrence Berkeley National Laboratory, Berkeley, California 94720, USA.

[7]Department of Chemical and Biomolecular Engineering, University of California, Berkeley, California 94720, USA.

Abstract

The ability to predict and control the formation of bimetallic heterogeneous nanocrystals is desirable for many applications in plasmonics and catalysis. Here, we report the synthesis and characterization of stable, monodisperse, and solution-processed Cu-Ag bimetallic nanoparticles with specific but unusual elemental arrangements that are consistent with a recently

developed thermodynamic model. Using air-free scanning transmission electron microscopy with energy dispersive X-ray spectroscopy, the distribution of Cu and Ag positions was unambiguously identified within individual nanocrystals (NCs), leading to the discovery of a Cu-Ag nanocrescent shape. A simple yet versatile thermodynamic model was applied to illustrate how the interplay between surface and interface energies determine the particle morphology. It is found that there exists a range of surface-to-interface energy ratios under which crescent-shaped nanocrystals are the thermodynamically favored products, with the morphology tunable by adjusting the Ag content. We further show the conversion of Cu-Ag nanocrescents into Ag@Cu_2O upon mild oxidation, whereas fully core-shell Cu@Ag NCs are robust against oxidation up to 100 °C. The plasmonic and interband absorptions of Cu-Ag NCs depend on the composition and the degree of Cu oxidation, which may find application in light-driven catalysis.

Introduction

The physical properties of metals, such as binding energies or plasmon resonance, can be significantly modified by forming nanoscale alloys and intermetallics.[1,2] While there are many theories developed for predicting the stability of a given bulk alloy as well as its structural and electronic properties,[3,4] the behavior of nanomaterials cannot be understood without considering surface and interface effects.[5] From a theoretical standpoint,

bimetallic nanocrystals are particularly intriguing and challenging due to the complexity of the formation energy landscape. Atoms of two metals order in a variety of patterns, ranging from single-phase homogeneous systems with either random or ordered mixing to multi-phase heterogeneous systems with segregated domains. The segregation can be further differentiated into structures, where atoms either order in uniform layers such that only one metal is present on the surface (core-shell) or instead form regions of many components present on the surface (e.g., bifacial Janus particles).[6] Hence, the ability to predict, and ideally control, the formation of segregated systems is crucial for surface-specific applications.[7]

Here, we report the synthesis, characterization, and theoretical considerations of a new family of stable, monodisperse, and solution-processed Cu-Ag bimetallic nanoparticles with controlled atomic arrangement. These include the formation of Cu/Ag nanocrescents that, to the best of our knowledge, have not been observed before. High-resolution electron microscopy combined with elemental (EDS) mapping was applied to resolve the location of Cu and Ag within each of the structures. The bulk Cu-Ag system has been the subject of numerous phase-stability calculations, and is representative of segregated alloys with positive enthalpy of mixing.[8] Additionally, Cu-Ag bimetallic nanoparticles find applications in such fields as catalysis[9,10] and printed electronics.[11] As such, we decided to investigate whether the formation of bimetallic NCs of Cu and Ag can be predicted with a simple thermodynamic model focused on surface and interface effects. We

have revisited models studying wetting in multiphase systems[12–14] to probe how the geometry of Cu and Ag domains in a nanoparticle is primarily determined by the ratio of surface and interface energies. Here, surface energy refers to the energy needed to create a boundary between a solid and a vapor,[15] while interface energy is the cost to create an interface between two different solids.[16] By combining experimental results with a simple theoretical treatment, we hope to develop design principles for achieving desired geometries of binary NCs.

Cu-Ag bimetallic nanoparticles have been previously synthesized using pulsed laser deposition,[17] microwave irradiation,[18] and wet chemistry, both in aqueous[19] and organic[20,21] solvents. However, in most of these cases, the reports describe only one geometry of nanoparticles, either core-shell[11,20] or bifacial,[21,22] under the implicit assumption that there should exist one equilibrium product for the Cu-Ag bimetallic NC. Here, we present synthetic conditions that can produce multiple surface configurations: Ag only (core-shell), both Cu and Ag (crescent), and Cu only (as Cu_2O in an inverted core-shell). We also demonstrate that these various geometries are expected to occur at equilibrium, given specific and reasonable ratios of surface and interface energy values. An Organic-based synthesis was chosen, as it results in small (~7nm) nanoparticles, which emphasizes surface effects. Furthermore, the growth process was split into two steps to achieve better control over the system and to develop a more universal synthetic scheme. First, Cu particles were synthesized, and afterward, Ag salt was added to

induce galvanic exchange at low (<100 °C) temperatures. Galvanic exchange is driven by the reduction potential between Cu and Ag, since Cu atoms are readily oxidized and replaced in the nanoparticles by reduced Ag.[23]

Galvanic exchange has been used for the synthesis of Cu-Ag nanoparticles before, yielding either core-shell[20] or clustered[21] geometries. What drives the choice between the two morphologies has not been explored previously. High-resolution STEM-EDS mapping under conditions that carefully exclude oxygen and avoid any air exposure is important, if not essential, for unambiguous identification of the location and Cu and Ag within the bimetallic nanomaterials. Cu readily oxidizes to Cu_2O, and this transformation is accompanied by significant restructuring of the particles. While it is possible to measure d-spacing from high-resolution TEM images, the d-spacing of Cu(111) and Ag(200) differ from each other by less than 0.05 Å, introducing substantial uncertainty into resolving HRTEM images. Using air-free STEM-EDS, we were able to unambiguously resolve the formed structures and separate the influence of oxidation on the morphology. Based on the temperature, two oxidized products were obtained, differing in particle geometry and the amount of Cu_2O.

Materials and Experimental Methods

Materials

Copper(I) acetate (Sigma-Aldrich, 97%), n-tetradecylphosphonic acid (further abbrev. as TDPA, Sigma-Aldrich, 97%), Trioctylamine (Sigma-Aldrich, 98%), Isoamyl ether (Sigma-Aldrich, 99%), Silver Trifluoroacetate (further abbrev. as Ag TFA, Sigma-Aldrich, ≥99.99% trace metals basis), Nitric acid (Sigma Aldrich, ≥99.999% trace metals basis), Water (Milli-Q, 18.2 MΩ), Hexane (Sigma-Aldrich, mixture of isomers, anhydrous, ≥99%), Ethanol (Sigma-Aldrich, pure, anhydrous, ≥99.5%), Isopropanol (Sigma-Aldrich, anhydrous, 99.5%), Tris(trimethylsilyl)silane (Sigma-Aldrich, 97%), Super-Hydride® solution (Sigma-Aldrich, 1.0 M lithium triethylborohydride in THF). All materials were used without further purification unless specified otherwise in the experimental methods.

Synthesis

Cu nanoparticle synthesis

Cu nanoparticles capped with TDPA (~7 nm diameter) were synthesized according to a literature procedure, with strict air-free handling procedures to avoid any risk of particle oxidation that could impact subsequent synthetic steps.[24] Briefly, trioctylamine was degassed in a Schlenk flask by heating at 90 °C under vacuum for an hour and then transferred and stored in a glovebox. In the same glovebox, 123 mg of copper(I) acetate, 139 mg of n-tetradecylphosphonic acid, and 10 mL of degassed trioctylamine were added

to a 25 mL three-neck flask equipped with a transfer valve. The solution was stirred in an argon environment on a Schlenk line and heated to 105 °C to ensure that all solids were dissolved. Then it was rapidly heated (approx. 2 °C/s rate) to 180 °C and kept at this temperature for 30 min. The reaction mixture was subsequently heated to 270 °C (approx. 2 °C/s rate) and kept at this temperature for another 30 min. The purplish red colloidal solution was cooled down to room temperature and the whole flask was transferred immediately into a glovebox for particle purification. Cu particles were precipitated by addition of 1:1 ethanol:isopropanol mixture (1.25 × the volume of particles solution) and centrifuged at 5,000 rpm for 5 minutes without air exposure. Particles were re-dispersed in hexane and the centrifugation step was repeated. For TEM imaging and general storage, particles were again re-dispersed in hexane, and for the galvanic exchange, they were re-dispersed in isoamyl ether. Throughout all this process, care was taken to avoid any exposure to air.

Cu/Ag bimetallic formation via galvanic exchange

Using the centrifugation/re-dispersion method described in the previous section, Cu particles were dissolved in isoamyl ether (previously dried and degassed by heating at 130 °C for an hour under argon) in the glovebox. Based on inductively coupled plasma optical emission spectrometry (ICP-OES), Cu concentration was about 3 mg/mL. Separately, silver trifluoroacetate solution in isoamyl ether was prepared (5 mg added per 1g

of ether). To initiate galvanic exchange, the solution of Cu particles (500 mg) was mixed with the Ag ether solution (100-700 mg). The maximum amount of Ag TFA was dictated by the trifluoroacetate anion that precipitated the particles in a concentration higher than approximately 12mM. The reaction time was 2 hr, and heating, if needed, was provided by a hot plate inside the glovebox. For example, Cu/Ag crescents (20 at%Ag) were synthesized by adding 250 mg Ag solution for 2 hr at 25 °C; a mixture of Cu/Ag and Cu@Ag (35 at%Ag) was obtained by adding 600 mg Ag solution for 2 hr at 25 °C; Cu@Ag core-shell NCs (60 at%Ag) were synthesized by adding two batches of 700 mg Ag solution, each time for 2 hr at 90 °C. At the end of the reaction time, particles were precipitated and re-dispersed in hexane, following the same procedure as in the previous section, or in isoamyl ether to add another batch of Ag TFA.

Particle oxidation and inversion to Ag@Cu_2O

Particles were oxidized at room temperature either by taking the hexane solution out of the glovebox and exposing it to air or by letting hexanes dry completely and having particles in direct contact with air. To accomplish a full conversion to Ag@Cu_2O, the solvent was evaporated outside of the glovebox and dry particles were heated for an hour at 90 °C. Afterward, particles were re-dispersed in hexane again.

Characterization

Electron Microscopy

Routine transmission electron microscopy (TEM) was done by drop-casting particles on a TEM grid (Electron Microscopy Sciences, CF-400-Cu) and acquiring images on a 200 kV Tecnai G2 T20 S-TWIN with a Gatan SC200 CCD camera. High-resolution (HRTEM) was acquired either on JEOL 2100-F or FEI TitanX, both operating at 200 kV. Selected area electron diffraction (SAED) patterns, as well as STEM-HAADF and STEM-EDS imaging were performed on FEI TitanX using a Fischione high-angle annular dark-field (HAADF) detector with an inner semi-angle, β, of 63 mrad. The EDS detector was the FEI Super-X windowless detector with a solid angle of 0.7 steradians. Bruker Esprit software was used for quantitative elemental analysis. To minimize carbon contamination, ultrathin carbon on gold TEM grids (Ted Pella, 01824G) were cleaned with oxygen-plasma right before drop-casting the particles. For oxygen-free imaging, the TEM grid was prepared and inserted into a TEM holder in a glovebox. The holder was then transported to the microscope inside a protective vacuum sheath in order to maintain the argon atmosphere until just before inserting into the microscope (<1 min exposure to air).

X-ray photoelectron spectroscopy

The core level, Auger, and valence band spectra of the CuAg bimetallic nanoparticles were measured using a Kratos Axis Ultra DLD x-ray photoelectron spectrometer (XPS). All spectra were acquired using

monochromatized Al Kα radiation (15 kV, 15 mA). Ar sputtering of the sample surface was avoided in order to prevent surface composition changes resulting from the nonequivalent sputtering rates of Cu and Ag. The ligands used to stabilize the nanoparticles prevented facile charge transfer to the glassy carbon substrate, which resulted in charge accumulation within the nanoparticles during the course of analysis. Charge neutralization was conducted by flooding the chamber with electrons at a current of 1.6 A, which was experimentally determined to be optimal for suppressing measurement artifacts arising from the accumulation of charge within the nanoparticles. Since it was not possible to use the C 1s edge for calibration, the kinetic energy scale of the measured photoemission spectra was instead calibrated by setting the Ag $3d_{5/2}$ binding energy to 368.25 eV. The actual oxidation state of Ag was determined by the presence of loss features and an asymmetric shape of the peaks, which is indicative of the metallic Ag(0) state.[25]

Other techniques

UV-VIS spectroscopy of nanoparticle colloidal suspension in hexane in air-free quartz cuvettes was performed using Shimadzu UV-3600 UV-VIS-NIR spectrophotometer. Absolute concentration of Cu and Ag in the solution was determined by inductively coupled plasma optical emission spectrometry

(ICP-OES) using Perkin Elmer ICP Optima 7000DV. ICP sample preparation was done after at least two rounds of centrifugation to ensure the absence of any salt precursors. The nanoparticles were digested in high-purity nitric acid and diluted with ultrapure water to reach the optimal concentration for the measurement (0.5-10 ppm).

Results and Discussion

Cu-Ag Crescent and Core-Shell Particle Formation via Galvanic Exchange

Cu-Ag bimetallic particles were formed via a two-step process: 1. organic-based synthesis of Cu particles, 2. galvanic exchange of Cu with an Ag-containing salt. Dividing the synthetic process into two steps gave us significantly higher control over the morphology, as compared to simultaneous reduction of Cu and Ag precursors. Since Cu and Ag do not alloy in the bulk and the interface energy between these two metals is positive, it is important to avoid homogeneous nucleation that would lead to the formation of separate Cu and Ag nanoparticles. This was achieved by conducting galvanic exchange in ether, a non-reducing solvent.

The first reaction step was the synthesis of 7 nm tetradecylphosphonate-capped Cu nanoparticles following a previously published protocol.[24] (Figure S1) For the second reaction step, galvanic exchange, both Cu particles and Ag precursor needed to be soluble in the same solvent. Isoamyl ether was selected, because it does not reduce

copper or silver ions, and it dissolves both TDPA-capped Cu nanoparticles and silver trifluoroacetate. In the absence of any other reducing agent, Ag^{+} ions can only react with Cu^{0} in the prepared solution. All reaction steps were performed under the protective argon atmosphere, either on a Schlenk line or in a glovebox, in order to prevent any Cu oxidation. Ag TFA is known to thermally decompose at approximately 120 °C.[26] Since we wanted to avoid the possibility of Ag homogeneous nucleation, this set a temperature limit for the galvanic exchange.

The incorporation of Ag into Cu particles was probed with two techniques: inductively coupled plasma optical emission spectrometry (ICP-OES) and electron microscopy. ICP-OES can determine the bulk ratio of Cu and Ag in the tested samples but does not provide information on the spatial arrangement of the two materials. To unambiguously analyze the morphology and elemental composition of products, high-resolution TEM and STEM-EDS elemental mapping were employed with care to ensure no exposure to oxygen or air (Figure 1). For all presented STEM-EDS maps, the average Cu:Ag ratio was consistent with the one obtained from ICP-OES (less

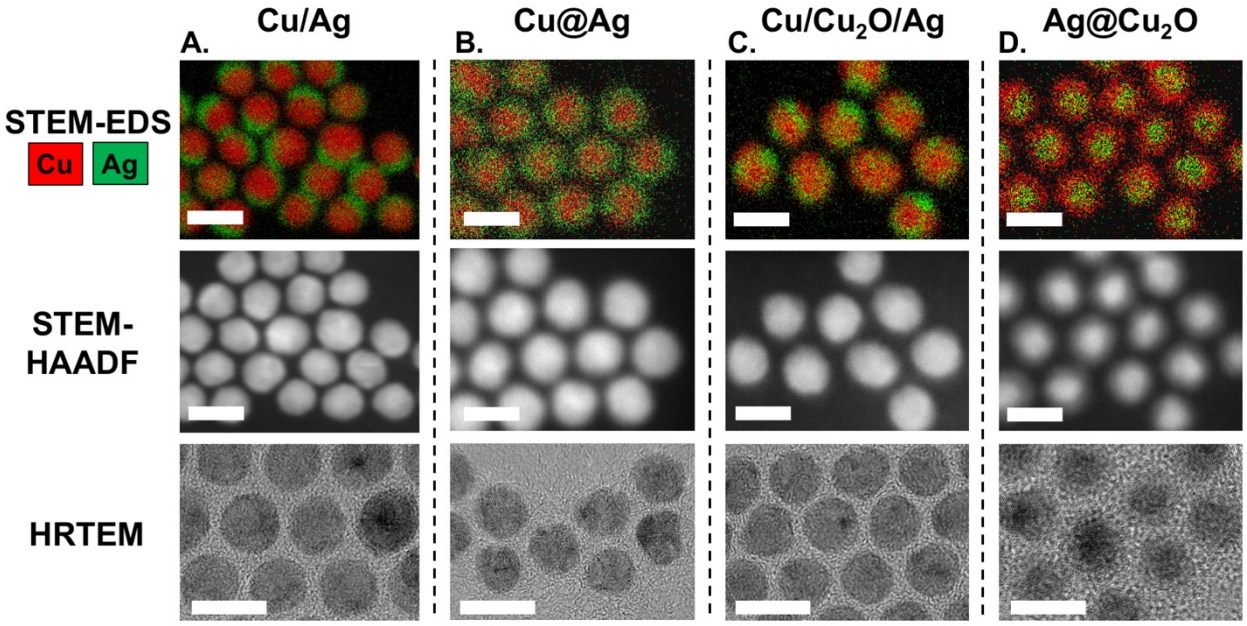

than 5% discrepancy, table S1), corroborating that the results presented here are representative of the entire sample.

Figure 1. Electron microscopy images of Cu-Ag bimetallic nanoparticles. Each row represents an electron imaging technique: STEM-EDS, STEM-HAADF, and HRTEM. All scale bars correspond to 10nm. Each column represents a different synthesized morphology. A: Cu/Ag nanocrescents (imaged in air-free conditions). B: Cu@Ag core-shell nanocrystals (imaged in air-free conditions). C: Cu/Cu_2O/Ag – Cu/Ag nanocrescents oxidized at room temperature. D: Ag@Cu_2O core-shell NCs synthesized by oxidizing nanocrescents at 90 °C.

Different conditions were probed for galvanic exchange by varying temperature and the relative concentration of Ag/Cu (Figure 2 A-D). Qualitatively, higher temperatures speed up the reaction, and higher concentrations of Ag salt result in a higher atomic fraction of Ag (at%Ag) in the bimetallic particles. The spatial distribution of Cu and Ag displays a more complex dependence on these two factors. While smaller amounts of Ag salt always favor the formation of an incomplete crescent-shaped shell (Cu/Ag) over the complete-shell (Cu@Ag), this relationship is also affected by the reaction temperature. At room temperature, slower diffusion rates result in more uniform coverage of particles. In contrast, at elevated temperatures (e.g., 90 °C), a heterogeneous population is more likely, with some particles having more Ag than the others (Figure S2). At higher temperatures, Ag

exchanges with Cu faster, leading to more heterogeneity. This is possibly due to the faster nucleation and dissolution rates at elevated temperatures, which lead to bigger Ag clusters and broader size distribution of the islands.[27]

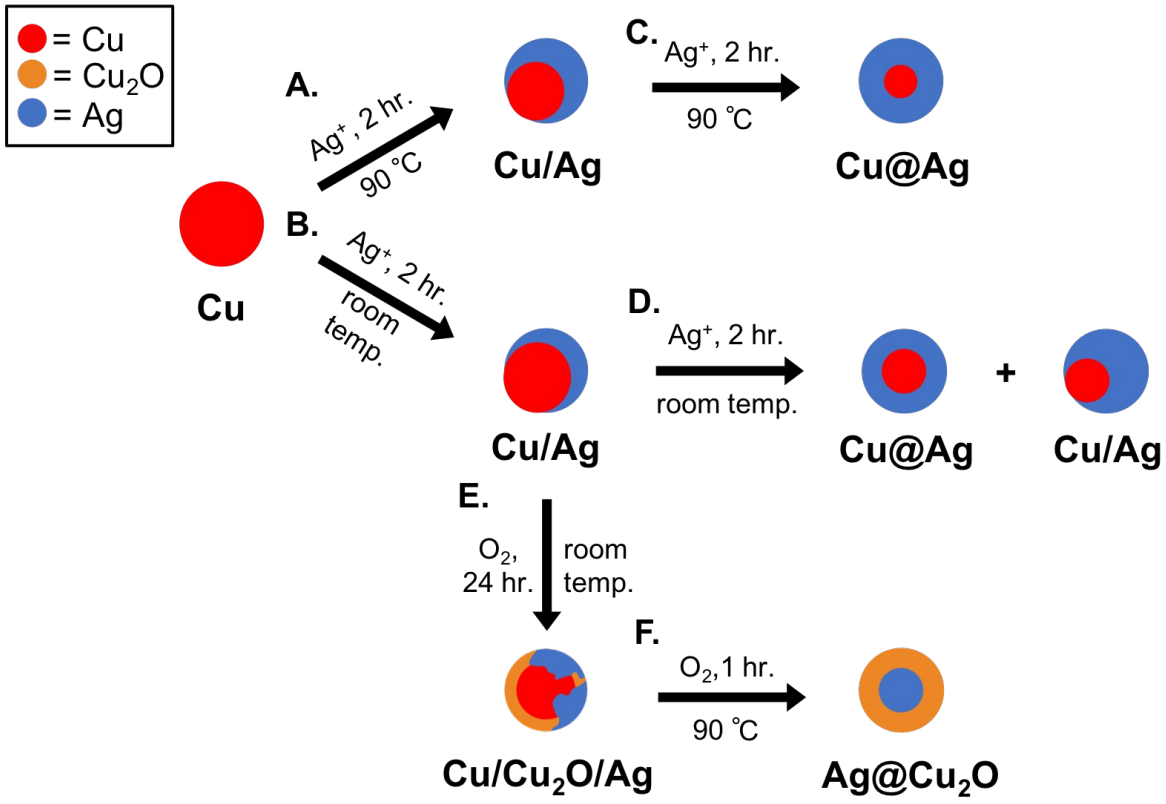

Figure 2. Reaction sequence for the synthesis of Cu-Ag bimetallic nanoparticles. A-B: Galvanic exchange of Cu nanoparticle with Ag^+ (at 25 °C and 90 °C) resulting in Cu/Ag crescents. C-D: Further addition of Ag^+ results in a formation of Cu@Ag particles or a mixture of Cu@Ag and Cu/Ag. In both cases, no more Ag can be incorporated. E: Exposure to oxygen at 25 °C oxidizes Cu to Cu_2O on the surface of the nanoparticles. F: Heating in air oxidizes Cu completely and inverts the morphology to $Ag@Cu_2O$.

When more Ag^+ is added to the nanoparticle solution or when the galvanic exchange initially starts with a larger Ag^+ amount, the shell coverage on the particles increases. Temperature dictates whether all particles can achieve complete-shell geometry. At 25 °C, at%Ag saturates at about 35% on average. At this ratio, some particles are fully core-shell, while others are locked in a crescent shape with an incomplete shell (Figure S3). As long as the galvanic exchange is kept at room temperature, further addition of Ag^+ does not change the Cu:Ag ratio. At 90 °C, we were able to synthesize Cu@Ag particles with 60 at%Ag on average, but only when the galvanic exchange with Ag^+ was performed twice. For particles fully covered in Ag, further galvanic exchange does not occur (as tested at both 25 °C and 90 °C), preventing further changes in Cu:Ag ratio. It is less apparent why the Cu/Ag crescents cannot incorporate more Ag. Possibly, due to strain arising from Cu-Ag lattice mismatch and energetics, no more Ag atoms can enter the particles, making the crescent structure the lowest energy configuration. The crescent geometry remains stable over long periods of time (at least one year), giving further evidence of its stability. A thin layer of cuprous oxide on the surface would also block galvanic exchange, but the particles have never been exposed to oxygen, so we doubt that this is the case.

Oxidation of Particles in Air

While it was crucial to synthesize and characterize the Cu-Ag nanoparticles without any exposure to oxygen for the comparison of theoretical and experimental results, we were also interested in the morphological changes induced by oxidation. In air, Cu nanoparticles invariably oxidize to copper oxide, but it is usually Cu(I), not Cu(II).[24,28] This oxidation dramatically changes the electronic and mechanical properties of copper.[11] However, researchers have demonstrated that adding Ag slows down oxidation rates.[21,29] For Cu@Ag, the mechanism of oxidation prevention is a simple one: Cu is covered with layers of Ag atoms, preventing contact with O_2 molecules. For particles with Cu atoms on the surface, the mechanism of oxidation prevention is more complex. DFT calculations suggest that as a result of a partial electron transfer from Cu to Ag, the affinity of Cu to O_2 decreases.[21] Recently, the reduction of oxygen binding energy of Cu has been experimentally observed for Cu-Ag bulk foils.[30]

During the galvanic exchange at 25 °C, as all Cu sites on the surface get oxidized, oxygen access is blocked and Cu(0) gets trapped underneath, resulting in Cu/Cu_2O/Ag geometries (Figure 2E). This phenomenon is analogous to the formation of Cu@Cu_2O from Cu, already observed for the monometallic nanoparticles used in galvanic exchange.[24] A more pronounced transformation occurs for Cu/Ag particles oxidized in air at 90 °C. At this temperature, the atomic mobility increases enough to fully oxidize Cu to Cu_2O and induce an inversion, from Ag being on the surface to Ag being exclusively enclosed in the core of Ag@Cu_2O particles (Figure 2F). This

reaction does not occur for Cu@Ag heated in air, nor Cu/Ag heated in the glovebox, indicating that temperature alone cannot change the morphology of Cu/Ag particles. Oxygen is necessary to bring Cu atoms on the surface of Ag, since Cu_2O is characterized by lower surface energy and larger lattice constant as compared to Ag[31,32]. As only Cu/Ag transform into Ag@Cu_2O upon heating, the observed inversion is useful in separating Cu/Ag from Cu@Ag.

To investigate oxidation states of Cu and Ag experimentally, X-ray photoelectron spectroscopy (XPS) and electron diffraction were used (see Figure S5 for the latter). XPS has the capacity of resolving oxidation states on the surface of the material, while electron diffraction, operating on the same principle as X-ray diffraction, identifies bulk crystal structure. Proper identification of surface Cu oxidation state is particularly difficult, as Cu(0) and Cu(I) cannot be reliably resolved using the principal line of the Cu 2p edge. Instead, Auger lines need to be used as they display a sufficient energy separation from each other.[33] Using XPS measurements, we were able to unambiguously confirm that Cu oxidizes primarily to Cu(I) (Figure 3); however, some Cu(II) is present on the surface (Figure S4a). Furthermore, the oxidation of dried Cu/Ag particles occurs on the timescale of hours at room temperature: particles left in air for only 2 hours still have mostly Cu(0) on the surface, and even after three days there is still some metallic Cu left. As expected, Ag@Cu_2O formed after oxidation at elevated temperatures shows only Cu(I) and Cu(II), while Cu@Ag primarily contains metallic Cu. Although technically XPS can probe the sample up to 10nm deep,[34] which is

more than the diameter of studied bimetallic particles, signal is strongest from the top-most layer, which explains why the Ag signal is stronger for Cu@Ag and weaker for Ag@Cu_2O, while the opposite is true for the Cu edges.

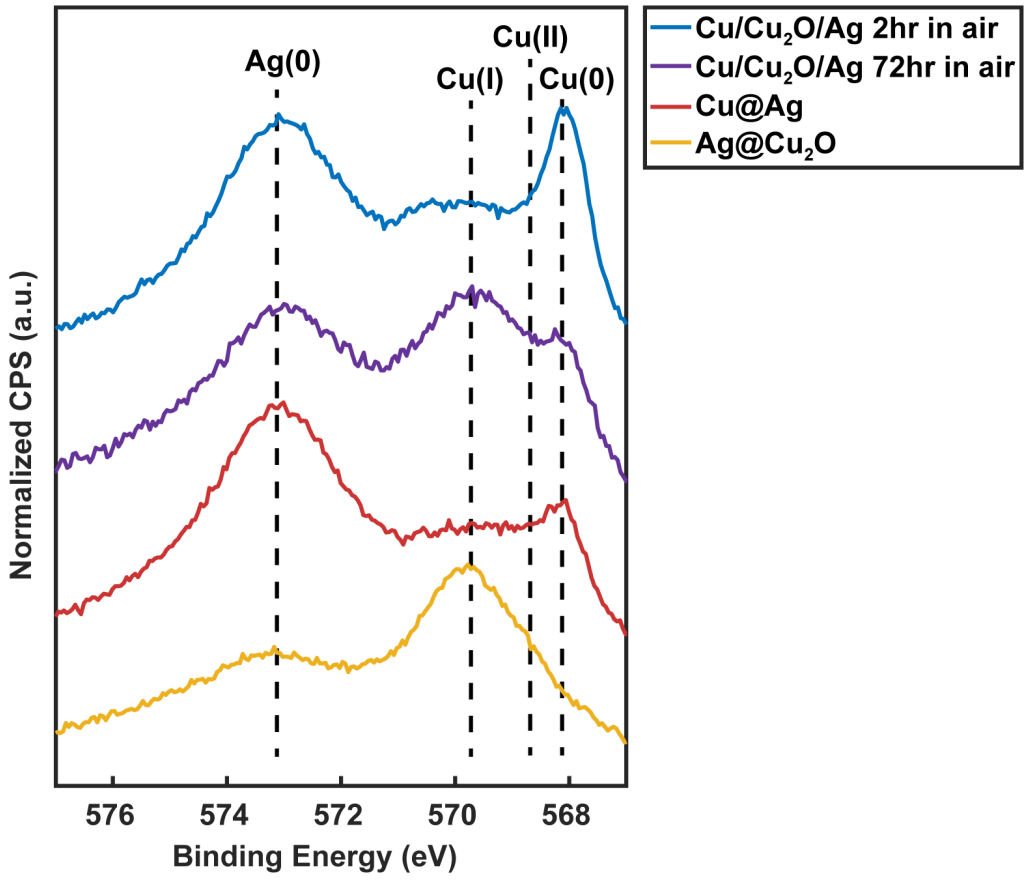

Figure 3. X-ray photoelectron spectroscopy spectra of Ag 3p and Cu LMM regions for Cu/Cu_2O/Ag (2 hr and 72 hr in air, respectively), Cu@Ag and Ag@Cu_2O.

Further information concerning Cu and its oxidation state came from the Cu 2p edge. At the Cu 2p edge, the resolution of Cu(0) vs. Cu(I) is uncertain, but Cu(II) displays a sufficient shift to be recognized (Figure S4a).

Unsurprisingly, Cu(II) is most abundant for Ag@Cu_2O, but this phase seems to be present to some extent in all samples. The Cu 2p edge also provided additional evidence for Cu(0) oxidation to Cu(I) based on the exact position of the main peak. According to literature, Cu(I) exists at slightly lower binding energy than Cu(0),[33] and indeed, Ag@Cu_2O is shifted by 0.3eV in relation to Cu@Ag (Figure S4a).

Regarding the oxidation state of Ag, there have been reports of Ag particles oxidizing in air, at least on the surface.[35] In this work, however, no substantial oxidation changes for Ag were observed, even during the transformation into Ag@Cu_2O. The Ag 3d edge of Cu@Ag had signal strong enough to show the loss features that are only present for Ag(0) (Figure S4b).[25] While other spectra did not have the signal strength required to observe the loss features, all Ag 3p edges displayed the same asymmetric shape which again indicated the presence of Ag metal.[25] The observed lack of Ag oxidation for Cu-Ag bimetallic particles may be caused by a large difference in the formation energies of Ag_2O and Cu_2O, which significantly favors the formation of the latter.[17] Furthermore, any molecular oxygen coming in contact with Ag atoms is likely to move towards Cu domains, due to the binding energy differences.[36]

Finally, it is worth mentioning that the transformation into Ag@Cu_2O seems irreversible. Reversing the oxidation of Cu to Cu_2O was attempted by exposing Ag@Cu_2O to three reducing agents: Tris(trimethylsilyl)silane (TTMSS), carbon monoxide and lithium triethylborohydride ($LiEt_3BH$, Super-

Hydride®). While TTMSS and CO were used at temperatures above 100 °C, according with previous literature reports,[37,38] $LiEt_3BH$ is potent enough to reduce Cu salts at room temperature. Nevertheless, none of these agents succeeded in obtaining Ag@Cu particles. Instead, we observed Cu etching and dewetting of the metals, resulting in pure Ag particles (former cores) remaining. Such results demonstrate the importance of surface energies and lattice strains in dictating particle morphologies. Metallic Cu has a significantly smaller lattice than metallic Ag does, while the surface energy of the latter is much larger than that of the former. Therefore, Cu(0) cannot accommodate a Ag(0) core underneath it, and the existence of Ag@Cu morphology for particles smaller than 10 nm is very unlikely.[6,39]

Optical Properties

While both Cu and Ag feature plasmonic responses, the two metals possess significantly different onset energy for interband transitions resulting in an interesting optical behavior when the two metals are in close contact.[22] The Cu-Ag optical properties are attractive for theoretical considerations as well as potential applications, such as light-driven catalysis.[22,40] The optical extinction spectra obtained for our Cu-Ag bimetallic nanoparticles are in good agreement with previous reports.[17,22] As Ag is introduced into the particles, a strong resonance feature appears and redshifts towards the standard Ag absorption (for <10 nm particles) of around 410 nm. At the same time, the Cu feature (~570 nm) fades away and eventually completely disappears (Figure 4a). Absorption peaks for Cu-Ag are broadened and

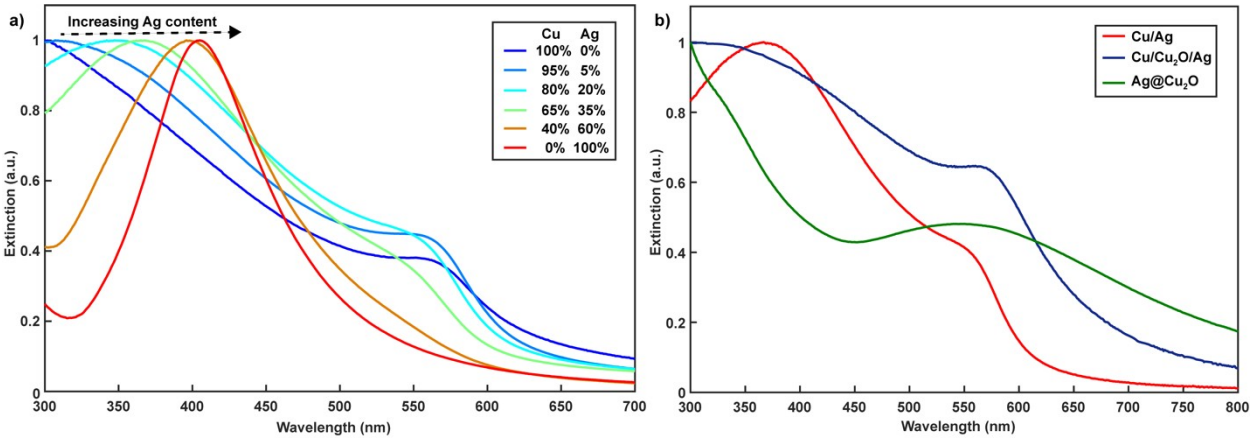

dampened as compared to monometallic particles.

Figure 4. a) Optical extinction spectra of unoxidized Cu-Ag bimetallic particles together with monometallic Cu particles (used for the galvanic

exchange) and Ag particles of the same size (~7 nm)[41] for comparison. b) Optical extinction spectra of Cu-Ag crescents (20 at%Ag) before and after oxidation in air. Spectra are normalized to the maximum peak.

As metallic Cu turns into semiconducting Cu_2O, the optical extinction undergoes significant changes (Figure 4b). These changes can only be observed for Cu/Ag crescents, where Cu is on the surface and prone to oxidation, as Cu@Ag does not oxidize. It is well-reported that the metal cluster oxidation is responsible for a redshift, which moves the Cu plasmon peak from approximately 570 nm to 590 nm.[24,42] The damping of both resonances can be explained and modeled by the formation of an outer oxide shell of large refractive index with the correlated size reduction of the remaining metallic core.[17] Indeed, the dampening is stronger for Ag@Cu_2O than for the Cu/Cu_2O/Ag sample. The presence of the oxide is also characterized by an increasing absorption in the infrared. This increasing infrared absorption (>700 nm), caused by the direct forbidden bandgap of Cu_2O,[43] is perhaps the most easily identifiable sign of the degree of particle oxidation.

The plasmon shift tied to the Cu:Ag ratio provides useful information during the synthesis process. Measuring the optical extinction is a much faster and accessible way to observe the galvanic exchange in Cu-Ag formation than imaging with an electron microscope. Although the latter provides more direct structural information and STEM-EDS is a technique

that allows unambiguous material characterization, UV-Vis (especially combined with ICP-OES) can serve as a quick identification tool for more routine syntheses. In the future, the plasmon shift could be useful for a catalytic application that requires the absorption center to be at 350-370 nm instead of 400 nm and above, as it is the case with pure Ag. As the resonance feature disappears as a result of Cu_2O formation, reducing and air-free environments, e.g., CO_2 reduction, may be best suited for light-driven Cu-Ag catalysis.

Thermodynamics of Crescent vs. Core-Shell Formation

Since Cu and Ag can hypothetically arrange in a variety of different morphologies, this system is a good model case for determining the equilibrium geometry based on the thermodynamics of surface and interface energies. However, thermodynamic equilibrium models are not applicable for kinetically-trapped products that change over time.[44] To the best of our knowledge, the existence of well-controlled Cu-Ag crescents has not been reported yet, so we wanted to confirm that the synthesized particles are equilibrium products and their shape can be elucidated with a model based on thermodynamics.

In the past, researchers observed dewetting of Ag from Cu@Ag particles over the course of one year.[20] Nevertheless, Cu/Ag crescents synthesized with our method do not seem to be undergoing any such changes. A 1-year-old sample, heated overnight at 100 °C in a glovebox (dissolved in isoamyl ether), shows no morphological change under STEM-EDS (Figure S6). While it is only suggestive, and not a complete proof that Cu/Ag crescents are indeed in a quasi-equilibrium instead of being kinetically-trapped, it certainly shows that inducing Ag dewetting is significantly harder than in the previous cases. The discrepancy may come from synthesizing the particles in the presence of different solvent and ligands or because of incidental partial oxidation. As it will be demonstrated, crescents can be equilibrium structures of the nanoparticle synthesis.

Inspired by a simple thermodynamic model,[14] we aimed at calculating the specific shape of a Cu-Ag crescent and the energy difference between various geometries. While the model described in reference 14 is general, we apply this model to our specific Cu-Ag system. Differences in interface/surface energies for different facets are ignored, and it is assumed that there is no stress at the interface. As the surface energy of Cu is significantly larger than that of Ag (for example $\gamma_{Cu(111)}$ = 1.83 J/m^2 and $\gamma_{Ag(111)}$ = 1.25 J/m^2),[32] it is reasonable to exclude Ag@Cu as a possible equilibrium product. Therefore, θ, the angle of the Ag coverage on Cu, is a good descriptor of the different idealized Cu-Ag shapes: separated monometallic Cu and Ag, crescent (Cu/Ag) and core-shell (Cu@Ag) (Figure 5). During galvanic exchange, Ag atoms can either homonucleate forming sep Ag particles (θ = 0°) or grow on top of the Cu core (θ > 0°). There's an energetic dri lowers the surface energy of the entire pa reasing amount of the unfavorable Cu-Ag int e mismatch between the two el wit vity difference.[8] These interactions create an for the possible existence of either Cu/Ag (θ < 180°) or Cu@Ag (θ = 180°).

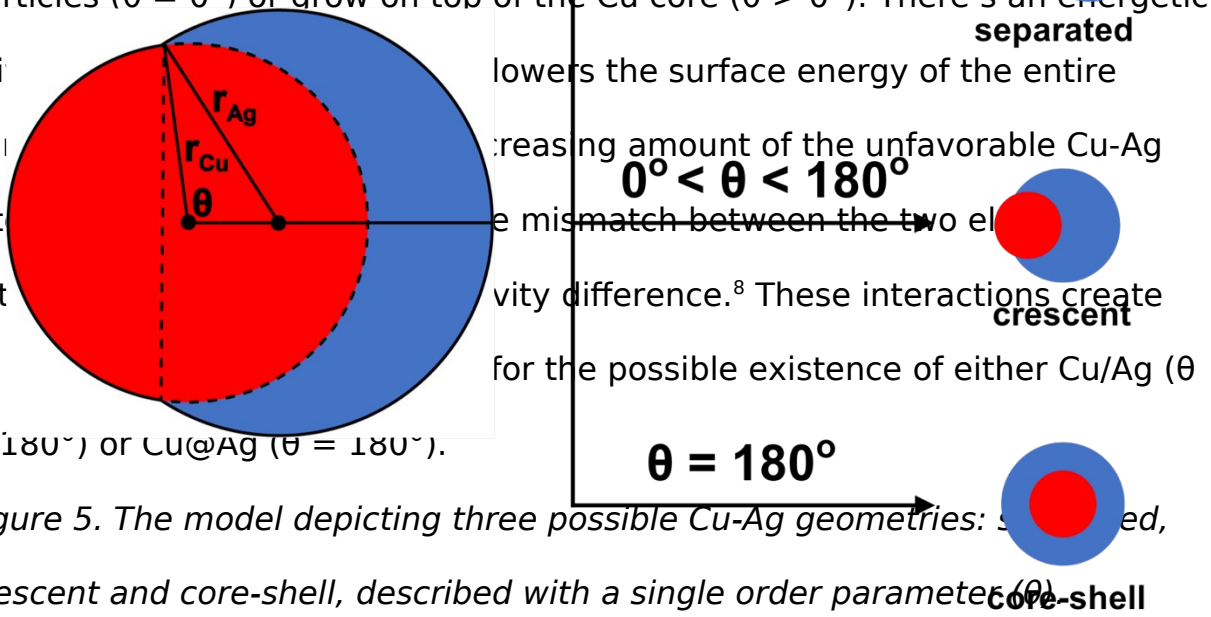

Figure 5. The model depicting three possible Cu-Ag geometries: s ed, crescent and core-shell, described with a single order parameter (θ).

For small particles, especially smaller than 10nm in diameter, surface and interface energies, i.e., quantities scaling with area, not volume, begin to dominate the energetic landscape.[45] The presented model considers only structures and energies of spheres and spherical caps. The Cu core is always represented by a sphere, while the geometry of the incomplete shell of Ag is represented by spherical caps that depend on the interplay between different surface energy terms (see SI for more details). For any given Cu:Ag ratio, the radius of the Cu core (r_{Cu}), and the angle θ, there is only one possible configuration in the model.

As long as there is a constant amount of Cu and Ag in the system, the cohesive energy, which scales with volume, cancels out. Under this condition, the simplest yet informative model needs to incorporate only three values: γ_{Cu} and γ_{Ag}, the surface energies of Cu and Ag, and γ_{Int}, the Cu-Ag interface energy. All these energies depend on a given facet,[32] but as long as perfect spheres are considered, there is no faceting involved, and average surface energy values suffice. The experimentally obtained particles do not display apparent faceting either (Figure 1), so this assumption seems appropriate. It should be noted that the surface and interface energies display size dependence for small nanoparticles, especially <5 nm in diameter.[46,47] When considering that size regime, it is prudent to apply a correction for the bulk energy values. However, the surface free energy of 7-8 nm size nanocrystals (Figure 1) differs from the bulk value by less than 5%.[46]

Surface and interface energies are positive, hence equilibrated structures will tend towards diminishing their overall contribution. Therefore, the most stable arrangement can be found by calculating total energies, i.e., summing up each γ multiplied by a corresponding surface area and finding the geometry with the minimum energy value (see SI for more details). As we intend for the model to elucidate the relationship between the surface and interface energies, instead of focusing on any specific values, the variables can be further simplified to $\gamma_{Cu} / \gamma_{Int}$ and $\gamma_{Ag} / \gamma_{Int}$. The calculated energy was then normalized by setting γ_{Int} to 1. This way, the model can be numerically solved for a range of values of γ_{Cu} and γ_{Ag} (Figure S7).

It has already been demonstrated that the crescent structure ($0° < \theta < 180°$) is energetically favorable for intermediate values of γ_{Cu}, γ_{Ag}, and γ_{Int}, namely $\gamma_{Cu} < \gamma_{Ag} + \gamma_{Int}$ and $\gamma_{Int} < \gamma_{Cu} + \gamma_{Ag}$.[14] However, the exact shape of the crescent, as well as the degree by which crescent geometry is more favorable than that of core-shell, depend on the specific Cu:Ag ratio (Figure 6). When the at%Ag is small, the optimal θ is also small and the crescent is the equilibrium shape. On the other hand, for particles mainly composed of Ag, the thermodynamic preference between a crescent and a core-shell structure is greatly diminished. This theoretical relationship corresponds with the experimental results. Experimentally, at approximately 20 at%Ag, all synthesized particles are clearly in the crescent shape, but at 35 at%Ag, both crescents and core-shell can be observed (Figure 2).

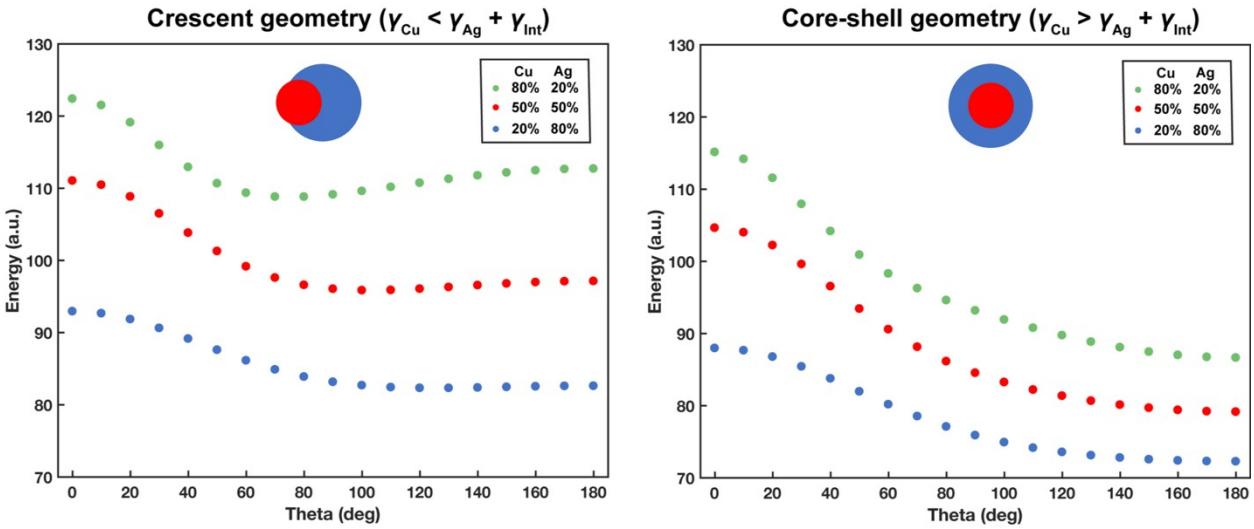

Figure 6. Calculated energies for two sets of γ_{Cu}, γ_{Ag}, and γ_{Int} for three different atomic ratios of Cu:Ag that lead to either crescent geometry, with the minimum energy value corresponding to an intermediate value of θ (left) or core-shell geometry, where θ =180° has the lowest energy (right).

Regarding valid parameter ranges in the model, the consideration of γ_{Cu} being either smaller or greater than the sum of γ_{Ag} and γ_{Int} is not a hypothetical one. While γ_{Cu} is always larger than γ_{Ag}, molecular dynamics (MD) calculations show that based on the facets, the interplay of surface and interface energies can result either in crescent or core-shell being the equilibrium structure, i.e., either $\gamma_{Cu} < \gamma_{Ag} + \gamma_{Int}$ or $\gamma_{Cu} > \gamma_{Ag} + \gamma_{Int}$, respectively.[48] For example, Cu(111) interfacing with Ag(111) should form a core-shell structure (since $\gamma_{Cu} > \gamma_{Ag} + \gamma_{Int}$ according to the MD calculations),[48] but if the interface is positioned on (100) facets (i.e., $\gamma_{Cu} < \gamma_{Ag} + \gamma_{Int}$), then one would expect a formation of crescents. It is generally assumed that the Cu-Ag interface occurs along lowest-energy facets, i.e., (111),[6] but often

these energies are calculated based on bulk surfaces. They do not include curvature and surface effects, which are very important for small nanoparticles. It should also be remembered that theoretical calculations often do not consider ligands, which can change the surface energies.[49] The γ_{Cu} and γ_{Ag} relevant for the thermodynamic model correspond to surfaces capped with TDPA, not for bulk surfaces in vacuum. Nevertheless, the model suggests that the average interface between the two metals in Cu/Ag crescents more closely resembles that of (100) facets than (111).

The same type of thermodynamic analysis can be performed for Ag@Cu_2O, which also consists of only two materials. Although we could not find a calculated value for the interface energy between Ag and Cu_2O for any facets in the literature, the fact that only core-shell structures were observed at elevated temperatures leads to the conclusion that $\gamma_{Ag} > \gamma_{Cu2O} + \gamma_{Int}$. In other words, the surface energy of Cu_2O must be significantly lower than that of Ag (calculated $\gamma_{Cu2O(111)} = 0.71$ J/m^2 vs. $\gamma_{Ag(111)} = 1.25$ J/m^2)[31] or the interface energy between these two materials, γ_{Int}, is relatively low. Since Cu_2O and Ag have less of a lattice mismatch than Cu and Ag do, and there have been reports of epitaxially-grown Cu_2O on Ag,[50] γ_{Int} between the two materials should indeed be small, corroborating the simple thermodynamic model.

The two trends, smaller θ and stronger preference for crescent over core-shell for lower at%Ag, are true for all values from the intermediate regime of $\gamma_{Cu} < \gamma_{Ag} + \gamma_{Int}$ and $\gamma_{Int} < \gamma_{Cu} + \gamma_{Ag}$ (Figure S7). We consider the Cu:Ag ratio to be particularly relevant since it can be directly controlled in

experimental settings. Surface energies can be modified by changing the size of particles (especially for <5 nm in diameter)[46] or the binding ligand,[49] but the exact dependence of γ_{Cu}, γ_{Ag}, and γ_{Int} on these alterations is complex and experimentally challenging. On the contrary, adjusting the Cu:Ag ratio is relatively easy, simply by bringing more Ag^+ into the reaction solution (although only as long as there is Cu remaining on the nanocrystal surface for galvanic exchange).

With this ability to control the Cu:Ag ratio, one can consider how it affects the likely geometry of the particles and create a simple phase diagram. For the most dynamic region of surface and interface energies, i.e., where the crescent shape is theoretically an equilibrium structure, the energy difference between various geometries can be investigated as a function of the atomic fraction of Ag. Under these assumptions, we distinguish three synthetic regimes based on the atomic fraction of Ag: crescents only, both crescents and core-shell, and core-shell only (Figure 7). Such division matches the experimentally obtained results (Figure 2). It is important to remember that our model does not include the cohesive energies of Cu and Ag, as we only intend to compare the energetic stability of different structures for a specific composition of the metals. Therefore, Fig. 7 is meant to illustrate the relative stability of possible geometric arrangements with the same at%Ag and emphasize the dependence of thermodynamic preference for crescent over core-shell on the atomic fraction of Ag. Since we control the concentration of Ag^+ added in our

experiments, this model seems appropriate to elucidate the structural features observed.

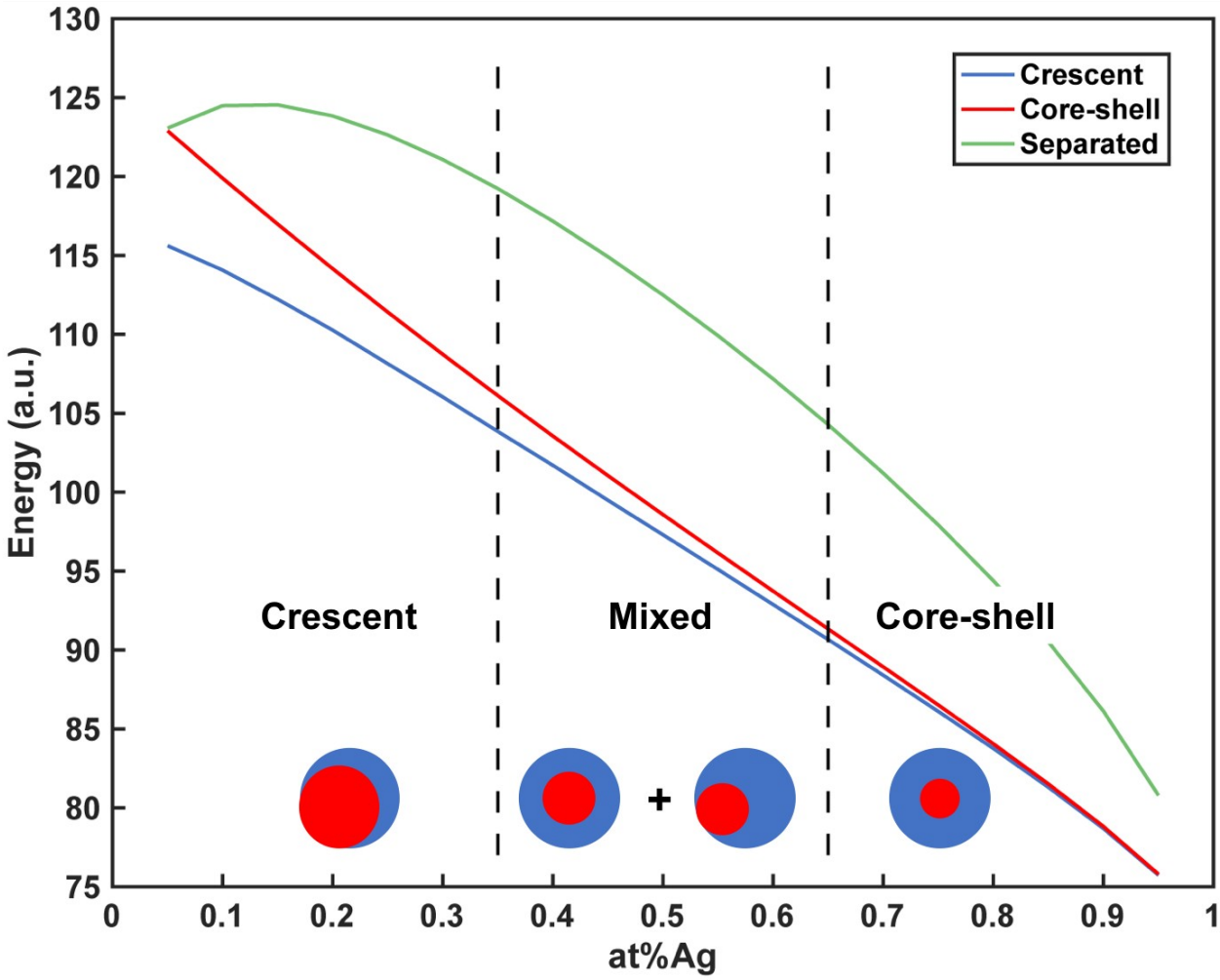

Figure 7. Calculated energies of three possible Cu-Ag shapes for different atomic fractions of Ag under the condition where the crescent is the equilibrium structure (i.e., $\gamma_{Cu} < \gamma_{Ag} + \gamma_{Int}$ and $\gamma_{Int} < \gamma_{Cu} + \gamma_{Ag}$). The three presented regimes correspond to experimentally observed structures, since the energy difference between crescent and core-shell varies with at%Ag.

The correspondence between the simple thermodynamic model and the experimental results is not perfect, as the model predicts that for a given set of γ_{Cu}, γ_{Ag}, and γ_{Int} there can be only one equilibrium geometry and it does not take into account entropic considerations. However, the consideration of the energetic difference between crescents and core-shell enables the creation of a framework for understanding how surface and interfacial energies affect the geometry of a bimetallic particle composed of two non-alloying metals at a given elemental ratio. Considering the ease of the thermodynamic model and its limited assumptions (perfectly spherical shapes, does not include any faceting and cohesive information), we find the insights offered to be highly instructive.

Conclusion

While precise predictions of geometries for nanoparticle syntheses are still challenging, the overall trends in binary Cu-Ag nanocrystal formation and the resulting phases were elucidated with a simple thermodynamic model that takes into account the counteracting forces of surface and interface energies. A part of this calculated phase diagram of Cu-Ag nanoalloys was experimentally explored to demonstrate that the same synthetic scheme can lead to both bifacial and core-shell geometries. Low atomic fractions of Ag favor the formation of nanocrescents, which have not been observed for this system before. High atomic fractions of Ag lead to more complete surface coverage, such that eventually only core-shell structures are formed. This

dependence leads us to believe that surface and interface energies of the system are in an intermediate range, i.e., $\gamma_{Cu} < \gamma_{Ag} + \gamma_{Int}$, according to the model predictions.

Using high-resolution elemental mapping, taking care to avoid oxygen and air exposure, the effect of oxidation on morphology was isolated and showed that temperature has a key influence on the degree to which Cu is oxidized to Cu_2O. At room temperature, some Cu(0) gets trapped in the core to form Cu/Cu_2O/Ag structures but 90 °C is sufficient to increase material mobility and results in an oxidative inversion to Ag@Cu_2O. The atomic fraction of Ag and the degree of oxidation significantly affect the optical behavior, resulting in changes in both absorption position and strength. The strong plasmonic response of Ag is dampened by contact with Cu, especially in its oxide form due to the semiconducting nature. The four synthesized and characterized structures (Cu/Ag, Cu@Ag, Cu/Cu_2O/Ag, Ag@Cu_2O) may find applications in fields such as catalysis, optics, and electronics, especially when a high degree of control over the surface elemental composition is needed.

Supporting Information

The Supporting Information is available free of charge on the ACS Publications website at DOI:

Additional electron microscopy images, atomic fractions of Cu and Ag in the nanoparticles, XPS data, electron diffraction patterns, mathematical details of the thermodynamic model of Cu-Ag nanoparticles.

Author Information

Corresponding author: paul.alivisatos@berkeley.edu

Acknowledgments

This work was supported by the U.S. Department of Energy, Office of Science, Office of Basic Energy Sciences, Materials Sciences and Engineering Division, under Contract No. DE-AC02-05-CH11231 within the Inorganic/Organic Nanocomposites Program (KC3104) and the Molecular Foundry. The authors appreciate conversations with Daryl Chrzan regarding the thermodynamic model in reference 14 as well as useful discussions with Wendy Gu, Jacob Kanady, Myoung Hwan Oh, Son Nguyen, Assaf Ben-Moshe, Hyun Dong Ha, Justin Ondry, Virginia Altoe, David Barton, Peter Nickias, Jaffar Hasnain, and Layne Frechette. XPS spectra were collected at the Joint Center for Artificial Photosynthesis, a DOE Energy Innovation Hub, supported through the Office of Science of the U.S. Department of Energy under Award Number DE-SC0004993.

References

(1) Ferrando, R.; Jellinek, J.; Johnston, R. L. *Chem. Rev.* **2008**, *108*, 845–910.

(2) Chaudhuri, R. G.; Paria, S. *Chem. Rev.* **2012**, *112*, 2373–2433.

(3) Pettifor, D. G.; Cottrell, A. H. *Electron Theory in Alloy Design*; Institute of Materials: London, 1992.

(4) Miedema, A. R.; de Boer, F. R.; Boom, R. *Calphad* **1977**, *1*, 341–359.

(5) Marks, L. D.; Peng, L. *J. Phys. Condens. Matter* **2016**, *28*, 053001.

(6) Peng, H.; Qi, W.; Li, S.; Ji, W. *J. Phys. Chem. C* **2015**, *119*, 2186–2195.

(7) Wang, D.; Li, Y. *Adv. Mater.* **2011**, *23*, 1044–1060.

(8) Ozolins, V.; Wolverton, C.; Zunger, A. *Phys. Rev. B* **1998**, *57*, 6427–6443.

(9) Wu, W.; Lei, M.; Yang, S.; Zhou, L.; Liu, L.; Xiao, X.; Jiang, C.; Roy, V. A. L. *J. Mater. Chem. A* **2015**, *3*, 3450–3455.

(10) Shin, K.; Kim, H.; Mo, H. *ChemSusChem* **2013**, *6*, 1044–1049.

(11) Lee, C.; Kim, N. R.; Koo, J.; Lee, Y. J.; Lee, H. M. *Nanotechnology* **2015**, *26*, 455601.

(12) Chatain, D.; Wynblatt, P.; Hagege, S.; Siem, E. J.; Carter, W. C. *Interface Sci.* **2001**, *9*, 191–197.

(13) Howe, J. M.; Mebed, A. M.; Chatterjee, K.; Li, P.; Murayama, M.; Johnson, W. C. *Acta Mater.* **2003**, *51*, 1359–1372.

(14) Yuan, C. W.; Shin, S. J.; Liao, C. Y.; Guzman, J.; Stone, P. R.; Watanabe, M.; Ager, J. W.; Haller, E. E.; Chrzan, D. C. *Appl. Phys. Lett.* **2008**, *93*, 4–6.

(15) Johnson, K. L.; Kendall, K.; Roberts, A. D. *Proc. R. Soc. Lond. A.* **1971**, *324*, 301–313.

(16) Cahn, J. W.; Hilliard, J. E. *J. Chem. Phys.* **1958**, *28*, 258–267.

(17) Pellarin, M.; Issa, I.; Langlois, C.; Lebeault, M.-A.; Ramade, J.; Lermé, J.; Broyer, M.; Cottancin, E. *J. Phys. Chem. C* **2015**, *119*, 5002–5012.

(18) Chen, Z.; Mochizuki, D.; Maitani, M. M.; Wada, Y. *Nanotechnology* **2013**, *24*, 265602.

(19) Tsuji, M.; Hikino, S.; Sano, Y.; Horigome, M. *Chem. Lett.* **2009**, *38*, 518–519.

(20) Muzikansky, A.; Nanikashvili, P.; Grinblat, J.; Zitoun, D. *J. Phys. Chem. C.* **2013**, *117*, 3093–3100.

(21) Kim, N. R.; Shin, K.; Jung, I.; Shim, M.; Lee, H. M. *J. Phys. Chem. C.* **2014**, *118*, 26324–26311.

(22) Wadell, C.; Yasuhara, A.; Sannomiya, T. *J. Phys. Chem. C.* **2017**, *121*, 27029–27035.

(23) Anderson, B. D.; Tracy, J. B. *Nanoscale* **2014**, *6*, 12195–12216.

(24) Hung, L. L.; Tsung, C. K.; Huang, W.; Yang, P. *Adv. Mater.* **2010**, *22*, 1910–1914.

(25) Pauly, N.; Yubero, F.; Tougaard, S. *Appl. Surf. Sci.* **2016**, *383*, 317–323.

(26) Szłyk, E.; Piszczek, P.; Chaberski, M.; Goliński, A. *Polyhedron* **2001**, *20*, 2853–2861.

(27) Madras, G.; McCoy, B. J. *Chem. Eng. Sci.* **2004**, *59*, 2753–2765.

(28) Yin, M.; Wu, C.-K.; Lou, Y.; Burda, C.; Koberstein, J. T.; Zhu, Y.; O'Brien,

S. *J. Am. Chem. Soc.* **2005**, *127*, 9506–9511.

(29) Chee, S.; Lee, J. *J. Mater. Chem. C* **2014**, *2*, 5372–5381.

(30) Clark, E. L.; Hahn, C.; Jaramillo, T. F.; Bell, A. T. *J. Am. Chem. Soc.* **2017**, *139*, 15848–15857.

(31) Soon, A.; Söhnel, T.; Idriss, H. *Surf. Sci.* **2005**, *579*, 131–140.

(32) Skriver, H. L.; Rosengaard, N. M. *Phys. Rev. B* **1992**, *46*, 7157–7168.

(33) Biesinger, M. C.; Lau, L. W. M.; Gerson, A. R.; Smart, R. S. C. *Appl. Surf. Sci.* **2010**, *257*, 887–898.

(34) Gilbert, J. B.; Rubner, M. F.; Cohen, R. E. *Proc. Natl. Acad. Sci.* **2013**, *110*, 6651–6656.

(35) Cai, W.; Zhong, H.; Zhang, L. *J. Appl. Phys.* **1998**, *83*, 1705–1710.

(36) Besenbacher, F.; Nørskov, J. K. *Prog. Surf. Sci.* **1993**, *44*, 5–66.

(37) Cui, F.; Yu, Y.; Dou, L.; Sun, J.; Yang, Q.; Schildknecht, C.; Schierle-Arndt, K.; Yang, P. *Nano Lett.* **2015**, *15*, 7610–7615.

(38) Kang, Y.; Ye, X.; Murray, C. B. *Angew. Chemie - Int. Ed.* **2010**, *49*, 6156–6159.

(39) Delogu, F. *J. Phys. Chem. C* **2010**, *114*, 19946–19951.

(40) Linic, S.; Christopher, P.; Ingram, D. B. *Nat. Mater.* **2011**, *10*, 911–921.

(41) Lin, X. Z.; Teng, X.; Yang, H. *Langmuir* **2003**, *19*, 10081–10085.

(42) Rice, K. P.; Walker, E. J.; Stoykovich, M. P.; Saunders, A. E. *J. Phys. Chem. C* **2011**, *115*, 1793–1799.

(43) Borgohain, K.; Murase, N.; Mahamuni, S. *J. Appl. Phys.* **2002**, *92*, 1292–1297.

(44) Tao, A. R.; Habas, S.; Yang, P. *Small* **2008**, *4*, 310–325.

(45) Yang, C. C.; Mai, Y. W. *J. Phys. Chem. C.* **2013**, *117*, 2421–2426.

(46) Xiong, S.; Qi, W.; Cheng, Y.; Huang, B.; Wang, M.; Li, Y. *Phys. Chem. Chem. Phys.* **2011**, *13*, 10648–10651.

(47) Qi, W. *Acc. Chem. Res.* **2016**, *49*, 1587–1595.

(48) Chandross, M. *Model. Simul. Mater. Sci. Eng.* **2014**, *22*, 075012.

(49) Puzder, A.; Williamson, A. J.; Zaitseva, N.; Galli, G.; Manna, L.; Alivisatos, A. P. *Nano Lett.* **2004**, *4*, 2361–2365.

(50) Jing, H.; Large, N.; Zhang, Q.; Wang, H. *J. Phys. Chem. C* **2014**, *118*, 19948–19963.

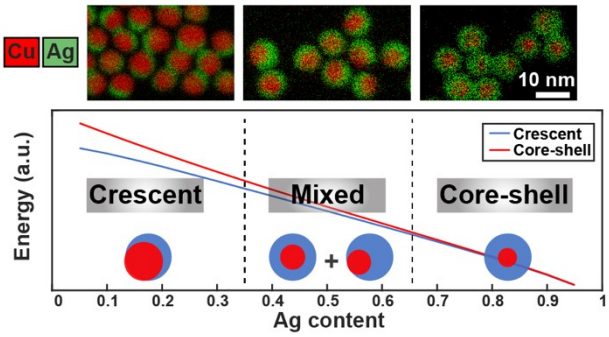

For Table of Contents Only